Proceedings World Geothermal Congress 2026
Calgary, Canada, June 8 – 11, 2026

Surrogate Modeling for Geothermal Thermal-Hydraulic Coupled Field Based on Physics-informed Neural Networks

Jialin Zhao[1,2], Junlin Yi[1,2], Gaosheng Wang[1,2,3]*, Xianzhi Song[1,2]*

[1]State Key Laboratory of Petroleum Resources and Engineering, China University of Petroleum, Beijing, Beijing 102249, China

[2]State Key Laboratory of Deep Geothermal Resources, China University of Petroleum, Beijing, Beijing 102249, China

[3]College of Energy Innovation, China University of Petroleum, Beijing, Beijing 102249, China

*wanggs@cup.edu.cn, songxz@cup.edu.cn

Keywords: Geothermal exploitation; Artificial intelligence; Neural networks; Surrogate model; Production prediction

ABSTRACT

Geothermal energy is a clean and renewable resource with sustainable development potential, utilizing artificial intelligence algorithms for geothermal resource extraction becomes an inevitable development trend. Traditional machine learning methods for predicting geothermal production suffer from low computational efficiency and poor transferability due to the lack of physical information constraints. Therefore, a two-dimensional surrogate model for geothermal Thermal-Hydraulic coupled field based on a Physics-Informed Neural Networks (PINNs) is established. The automatic differentiation method is employed, and the two-dimensional flow and heat transfer equations and geothermal reservoir parameters are embedded as constraints within the neural network. Two sampling methods are introduced to predict the temperature and pressure distributions near the injection and production wells after 20 years of operation period. The neural network is optimized by minimizing the loss function, and Thermal-Hydraulic coupled multi-physics field predicted by the trained surrogate model is compared with results from numerical simulation for validation and analysis. The results indicate that the Physics-Informed Neural Networks can learn a surrogate model with stronger generalization capabilities using fewer data samples. The trained model achieves minimum pressure MAE of 0.013 MPa (RMSE 0.04139 MPa) and a temperature MAE of 0.547 K (RMSE 1.429 K), demonstrating superior prediction performance that aligns more closely with field conditions. In the future, the approach presents a promising direction for future applications in multi-physical coupling and intelligent geothermal reservoir management.

1 INTRODUCTION

Geothermal energy is a clean and renewable resource characterized by high stability and independence from seasonal or climatic variations. As a promising alternative to fossil fuels, geothermal energy has attracted increasing global attention (Ji et al., 2025; Wang et al., 2022). Current geothermal development relies primarily on numerical simulation, including finite volume (Chen et al., 2021), finite element (Wei et al., 2013), and finite difference methods (Li et al., 2022). However, under complex geological structures and strong heterogeneity conditions, conventional numerical models often struggle to generate high-quality grids that accurately represent subsurface features, leading to low computational efficiency and poor timeliness. These limitations significantly hinder rapid forecasting during long-term geothermal reservoir production prediction. Therefore, developing a new modelling framework that simultaneously ensures high accuracy, strong generalization capability, and computational efficiency has become an urgent requirement for scalable geothermal development.

In contrast to traditional methods that rely on strict grid partitioning and numerical discretization, machine learning offers a data-driven means to automatically learn latent nonlinear relationships and extract key governing features from high-dimensional datasets, providing greater flexibility and efficiency for modeling complex geothermal systems (Ma et al., 2025). Recent studies have begun integrating intelligent models into geothermal resource assessment and operation forecasting. Yang et al. (2022) developed a deep belief network to identify the complex relations among 20 controlling factors and measured temperatures, enabling prediction of the subsurface thermal field. Shi et al. (2025) proposed an Fourier Neural Operator (FNO) model to capture the interplay between fracture-morphology variability and boundary-condition dynamics in geothermal

reservoirs. Despite their advantages in computational efficiency and nonlinear representation, data-driven models generally require large training datasets, limiting performance in small-sample scenarios. To overcome this limitation, Raissi et al. (2019) introduced physics-informed neural networks (PINNs), which embed governing physical laws into the loss function, thereby reducing dependence on abundant data and enhancing accuracy and interpretability. Jagtap et al. (2020) proposed a conservative PINN for solving high-dimensional nonlinear differential equations, including one- and two-dimensional Burgers equations and the KdV equations. Mao et al. (2020) applied PINNs to both forward and inverse Euler problems for simulating high-speed compressible gas flows. Zhang et al. (2022) further developed a GW-PINN framework that requires no labeled data to solve groundwater flow equations, demonstrating strong capability in capturing hydraulic head variations in both confined and unconfined aquifers.

Accordingly, the study proposes a deep learning framework based on PINNs to solve the coupled Thermal-Hydraulic transport partial differential equations in the geothermal reservoir. The model takes Two-dimensional spatiotemporal coordinates as inputs, and its loss function integrates the boundary, label data and partial differential equations residual terms, with hard boundary conditions imposed to enhance accuracy. Two sampling strategies are evaluated within the PINNs surrogate model to assess their suitability for geothermal pressure and temperature prediction. The pressure and temperature distributions after 20 years of production under various reservoir conditions are solved and validated against numerical simulation software results. The study provides references for future applications of surrogate models in geothermal energy.

2 GOVERNING EQUATIONS

In this study, the geothermal reservoir is treated as a continuous porous medium distributed over a two-dimensional spatial domain, where (x, y, t) denote the spatial and temporal coordinates. Fluid flow and heat transfer are assumed to satisfy the continuum hypothesis, Darcy's law and the mass conservation equation. The fluid flow is explained as follows:

$$-\frac{1}{\rho_f g}\nabla\cdot(K\nabla p)+\frac{\mu_s}{\rho_f g}\frac{\partial p}{\partial t}=W \tag{1}$$

$$\nabla p=(\frac{\partial p}{\partial x},\frac{\partial p}{\partial y})^T \tag{2}$$

$$K=kM \tag{3}$$

where p(Pa) indicates the fluid pressure, W(m/s) denotes the source term, and ρ_f (kg/m^3) is the fluid density. K(m^2/s) denotes the transmissivity, M(m) is the thickness of reservoir, and k (m/s) represents the hydraulic conductivity.

$$W=\sum_{i=1}^{N_{in}}Q_{in}\delta(x-x_i)-\sum_{j=1}^{N_{out}}Q_{out}\delta(x-x_j) \tag{4}$$

$$\delta(x)=\begin{cases}0 & x\neq 0\\ \infty & x=0\end{cases} \tag{5}$$

where Q_{in} represents the injection capacity of injection well located at (x_i, y_i); Q_{out} indicates the production capacity of production well located at (x_j, y_j); N_{in} and N_{out} denote the number of injection wells and production wells, respectively; δ is the Dirac delta function, which is defined by:

$$\int_{R^2}\delta(x)\,dx=1 \tag{6}$$

The local thermal equilibrium is adopted to describe the heat transfer process, which can be expressed as:

$$(\rho c_p)_{eff}\frac{\partial T}{\partial t}+\rho_f c_{p,f}u\mathrm{g}\nabla T-\nabla\mathrm{g}(\lambda_{eff}\nabla T)=-Q_E \tag{7}$$

$$\left(\rho c_p\right)_{eff}=(1-\varphi)\rho_s c_{p,s}+\varphi\rho_f c_{p,f} \tag{8}$$

$$\lambda_{eff}=(1-\varphi)\lambda_s+\varphi\lambda_f \tag{9}$$

where $(\rho c_p)_{eff}$ (J/(K·m^3)) is the effective volumetric capacity. λ_{eff} is the effective thermal conductivity. $c_{p,f}$ (J/(kg·K)) and λ_f denote the heat capacity and thermal conductivity of the reservoir fluid, respectively. ρ_s (kg/m^3) is the density of the reservoir solid component. $c_{p,s}$ (J/(kg·°C)) and λ_s (W/(m·°C)) indicate the heat capacity and thermal conductivity of the solid component, respectively.

3 PHYSICS-INFORMED NEURAL NETWORK

3.1 Network Architecture

The Physics-Informed Neural Networks (PINNs) architecture consists of an input layer, multiple hidden layers and an output layer, forming a fully connected feed-forward neural network. For each spatiotemporal point (*x*, *y*, *t*) the input vector is first transformed into a latent representation in the input layer and subsequently propagated through the hidden layers via linear transformations followed by nonlinear activation. The forward propagation from the (*k*-1)-th to the *k*-th layer can be described as:

$$a_j^k = \sum_i \omega_{ji}^k \sigma_{k-1}(a_i^{k-1}) + b_i^k \tag{10}$$

where ω_{ji}^k represents the weight connecting neuron *i* in the (*k*−1)-th layer to neuron *j* in the *k*-th layer k; b_i^k is the bias term of the k-th layer; $\sigma_{k-1}(a_i^{k-1})$ denotes the activation function associated with the (*k*−1)-th layer. Since the governing equations are second-order partial differential equations (PDEs), the network output must be at least twice differentiable with respect to the inputs. Thus, the twice-differentiable hyperbolic tangent function is adopted as the activation function.

The PINNs takes arbitrarily sampled spatiotemporal point (*x*, *y*, *t*) as the input and predicts the corresponding physical field value *u*(*x*, *y*, *t*; θ), where θ denotes the set of all trainable parameters. The training objective is to optimize θ so that the network output approximates the true solution *u*(*x*, *y*, *t*). These parameters are updated by minimizing a mean squared error (MSE) loss function, which is defined as:

$$L = L(u(x_i), u(x_i;\theta)) \tag{11}$$

$$\theta = \arg\min_{\theta} Loss(u(x_i), u(x_i;\theta)) \tag{12}$$

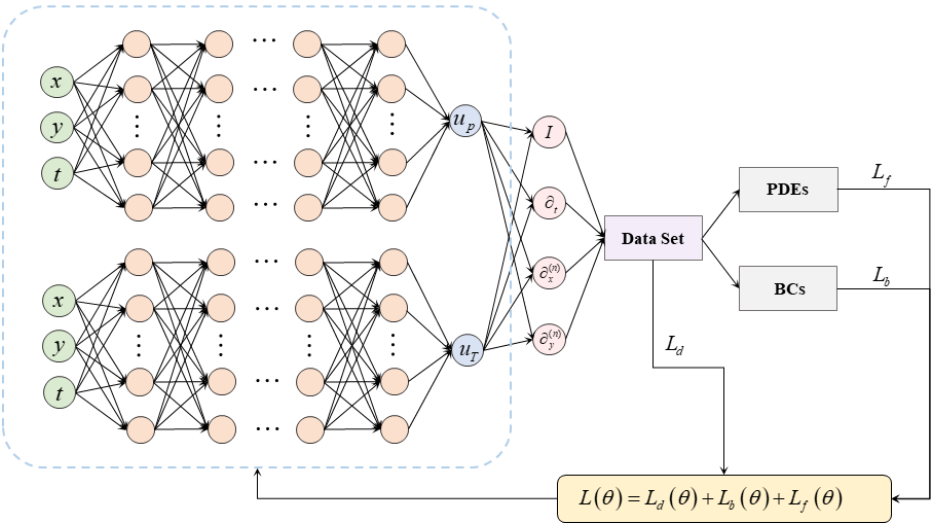


Figure 1. Basic architecture of the Physics-Informed Neural Networks

Considering the presence of both injection and production wells within the study area, source terms must be explicitly incorporated into the governing equations. In theory, such localized mass and heat exchange can be represented using a Dirac delta function $\delta(x, y)$. It is worth noting that the Dirac delta function is not differentiable everywhere, which is unfavorable for the calculation of high-order derivatives within an automatic differentiation framework. Therefore, in this study, a two-dimensional Gaussian density function is employed to construct a smooth approximation of the Dirac delta function, which is described as:

$$\delta(x,y)=\frac{1}{2\pi\sigma^2}e^{-\frac{\|x-y\|^2}{2\sigma^2}} \tag{13}$$

where σ denotes the standard deviation of the distribution. This treatment preserves the strongly localized nature of wellbore sources while ensuring spatial smoothness of the source term, thereby facilitating stable and accurate derivative computation within the PINNs framework.

3.2 Loss Functions

The loss function plays a central role in the training process of PINNs, typically consisting of data-driven and physics-based components. These terms are designed to balance observational fidelity and physical consistency, ultimately improving the model's generalization and reliability. In this study, the loss function is formulated to include the residuals of the coupled Thermal-Hydraulic (TH) governing equations L_f, various boundary conditions L_b and available observational data L_d. By jointly minimizing these components, the surrogate model achieves enhanced accuracy and generalization in approximating the pressure and temperature fields of the real Thermal–Hydraulic coupled multi-physics field processes, which are expressed as:

$$L(\theta)=L_d(\theta)+L_b(\theta)+L_f(\theta) \tag{14}$$

$$\begin{aligned}L_d(\theta)&=\frac{1}{N_d}\sum_{i=1}^{N_d}\left|\hat{u}\left(x_d^i,y_d^i,t_d^i;\theta\right)-u\left(x_d^i,y_d^i,t_d^i\right)\right|^2\\&=\frac{1}{N_d}\sum_{i=1}^{N_d}\left|\hat{u}_p\left(x_d^i,y_d^i,t_d^i;\theta\right)-u_p\left(x_d^i,y_d^i,t_d^i\right)\right|^2+\frac{1}{N_d}\sum_{i=1}^{N_d}\left|\hat{u}_T\left(x_d^i,y_d^i,t_d^i;\theta\right)-u_T\left(x_d^i,y_d^i,t_d^i\right)\right|^2\end{aligned} \tag{15}$$

$$\begin{aligned}L_b(\theta)&=\frac{1}{N_b}\sum_{i=1}^{N_b}\left|\hat{u}\left(x_b^i,y_b^i,t_b^i;\theta\right)-B\left(x_b^i,y_b^i,t_b^i\right)\right|^2\\&=\frac{1}{N_b}\sum_{i=1}^{N_b}\left|\hat{u}_p\left(x_b^i,y_b^i,t_b^i;\theta\right)-B_p\left(x_b^i,y_b^i,t_b^i\right)\right|^2+\frac{1}{N_b}\sum_{i=1}^{N_b}\left|\hat{u}_T\left(x_b^i,y_b^i,t_b^i;\theta\right)-B_T\left(x_b^i,y_b^i,t_b^i\right)\right|^2\end{aligned} \tag{16}$$

$$\begin{aligned}L_f(\theta)&=\frac{1}{N_f}\sum_{i=1}^{N_f}\left|\hat{u}\left(x_f^i,y_f^i,t_f^i;\theta\right)-f\left(x_f^i,y_f^i,t_f^i\right)\right|^2\\&=\frac{1}{N_f}\sum_{i=1}^{N_f}\left|\hat{u}_p\left(x_f^i,y_f^i,t_f^i;\theta\right)-f_p\left(x_f^i,y_f^i,t_f^i\right)\right|^2+\frac{1}{N_f}\sum_{i=1}^{N_f}\left|\hat{u}_T\left(x_f^i,y_f^i,t_f^i;\theta\right)-f_T\left(x_f^i,y_f^i,t_f^i\right)\right|^2\end{aligned} \tag{17}$$

The computational domain is divided into an interior region Ω and a boundary region Γ. The Dirichlet boundary condition is imposed on the pressure field, whereas the Neumann flux condition is applied to the temperature field. To ensure that the neural network outputs strictly satisfy the heterogeneous physical boundary constraints, this study incorporates a hard-constraint embedding strategy into the network architecture, aiming to avoid optimization difficulties caused by directly incorporating boundary conditions into the loss function.

For the Dirichlet boundary, the particular-solution construction proposed by Sun et al. (2020) is adopted. The formulation is expressed as:

$$u_p(x,y,t;\theta)=p(x,y,t)+d(x,y,t)u(x,y,t;\theta) \tag{18}$$

where $u(x, y, t; \theta)$ represents the output of the neural network; $p(x, y, t)$ is a function that satisfies the Dirichlet boundary and initial conditions; $d(x, y, t)$ is a smooth distance function representing the minimum distance from an interior point to the boundary. For any boundary point $(x_a, y_a, t_a) \in \Gamma$, the distance satisfies $d(x_a, y_a, t_a) = 0$, ensuring $u_p(x_a, y_a, t_a; \theta) = p(x_a, y_a, t_a)$. In contrast, for an interior point $(x_b, y_b, t_b) \in \Omega$, where $d(x_b, y_b, t_b) \neq 0$, the value of $u_p(x_b, y_b, t_b; \theta)$ is influenced by the boundary function $p(x_b, y_b, t_b)$ and the distance function $d(x_b, y_b, t_b)$.

4 RESULTS AND ANALYSIS

4.1 Simulation model setting

The training of the neural network in this study is implemented in PyTorch 2.2.1. The neural network consists of 7 hidden layers, with 32 neurons in each hidden layer. The sigmoid function is adopted as the activation function

and the Adam optimizer is used for training with an initial learning rate of 0.001. The results obtained at the end of training were compared with the simulation results from the finite element simulation software COMSOL, thereby verifying the solution accuracy of the PINNs.

To further assess the applicability of the proposed TH coupled PINNs surrogate model under varying well-pattern configurations, three representative geothermal development schemes were constructed, including a double-well system (Case 1), a three-well system (Case 2) and a four-well system (Case 3). All wells were placed within the computational domain Ω= [-500, 500] × [-500, 500]and the distributions of pressure and temperature fields after 20 years of continuous system operation were simulated. The injection and production rates for each well are listed in **Table 1**, while the corresponding COMSOL simulation results are presented in **Figure 2**.

Table 1. Flow rates of injection and production wells

Items	Values
Geothermal reservoir dimension	1000 m×1000 m
Initial pressure	50 MPa
Initial temperature	453.15 K
Permeability	10-150 mD
Porosity	0.1
Thickness of the aquifer	1 m
Injection rate	0.2 kg/s
Injection temperature	293.15 K
Injection-production spacing	300 m
Injection rate （Case1 and Case 3）	0.2 kg/s
Injection rate （Case2）	0.1 kg/s

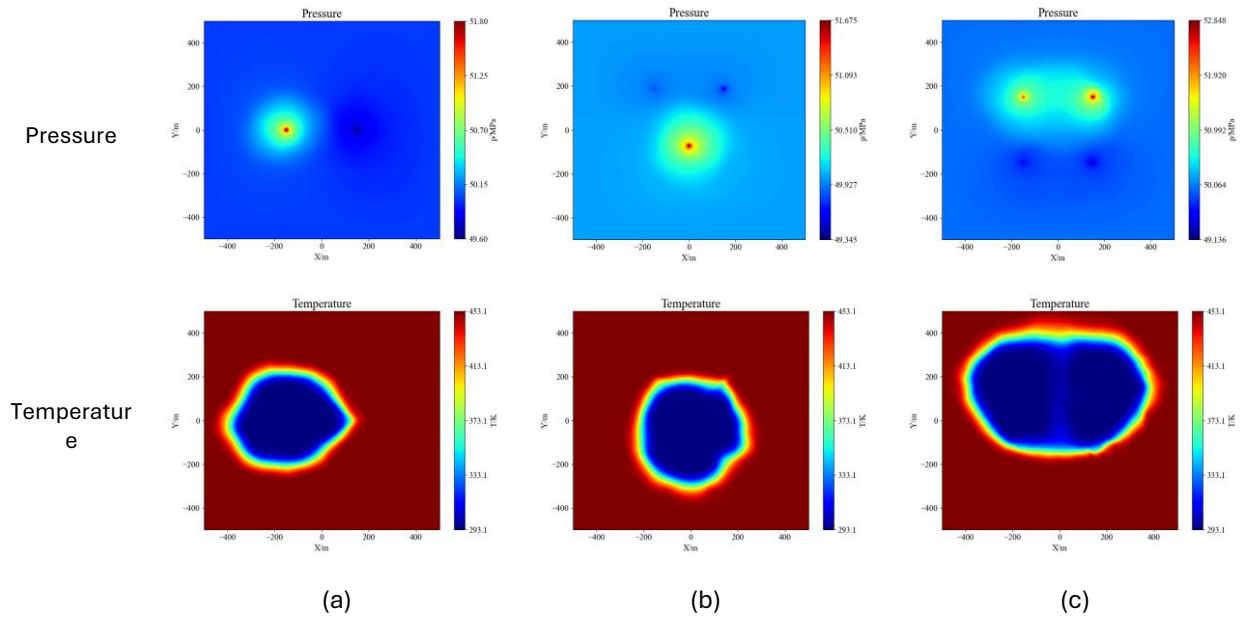
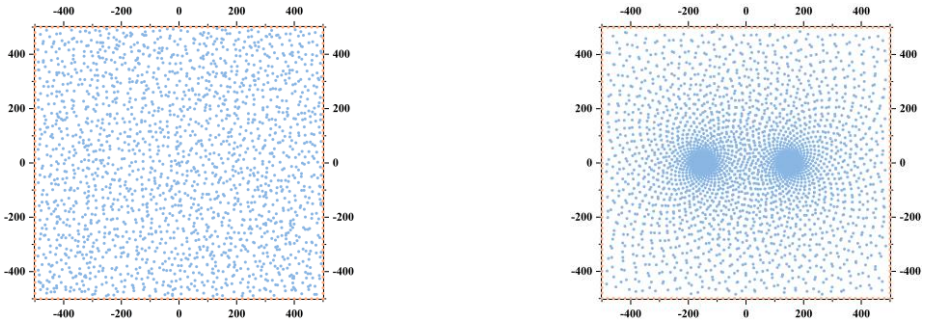


Figure 2. Numerical simulation results of pressure and temperature fields after 20 years of production (a) double-well system (Case 1) (b) three-well system (Case 2) (c) four-well system (Case 3).

An appropriate sampling strategy is essential for effective network training. Conventional random sampling may result in point clustering and insufficient coverage of the parameter space, thereby reducing the prediction

accuracy of the surrogate model. Lattice hypercube sampling (LHS) obtain comprehensive information on pressure and temperature fields by performing uniform sampling over the entire computational domain. However, steep gradients occur in the vicinity of injection and production wells, requiring additional resolution to accurately represent local variations. To address this, a locally refined sampling (LRS) strategy is adopted, enabling enhanced sampling density around wells and better characterization of sharp pressure and temperature evolution.

To evaluate the impact of sampling strategies, the study compared the accuracy of the PINNs in predicting reservoir pressure and temperature under the two sampling strategies. Taking the double-well system (one injection well and one production well) as an example, **Figure 3** illustrates the contrasting spatial distributions generated by the two sampling strategies.



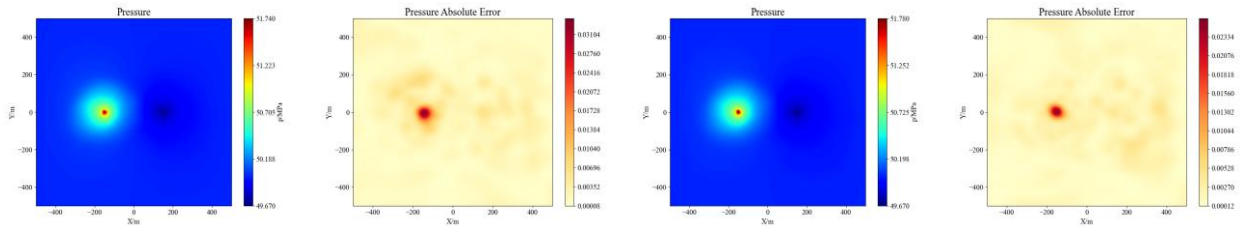
(a) (b)

Figure 3. Schematic diagram of sampling points (a) LHS (b) LRS

4.2 Model Testing Case

A total of 6000 data sampling points are generated using LHS and LRS and subsequently input into the neural network for training. **Figure 4** presents the contour maps of pressure, temperature and their corresponding errors in the double-well system after 20 years of production under the two sampling strategies. As shown in **Figures 4a** and **4c**, the injection well and the production well disrupt the stable pressure state of the reservoir, with the pressure variation zone mainly concentrated near the wells. The pressure is the highest at the injection well, forming a funnel-shaped zone that spreads outward and gradually decreases to the equilibrium pressure of the geothermal reservoir, while a distinct negative pressure region develops around the production well. Overall, the balanced injection of low-temperature fluid and extraction of high-temperature fluid ensures a long term of the production-injection balance within the system, preventing groundwater table decline and extending the operational lifespan of the geothermal reservoir. **Figures 4b** and **4d** illustrate the spatial distribution of pressure prediction errors, which are primarily concentrated near the injection well. This concentration arises from the steep pressure gradients and rapid variations in this region, where the surrogate model exhibits greater difficulty in accurately capturing the nonlinear pressure response close to high-gradient boundaries.

The contour maps of geothermal reservoir temperature in the double-well system after 20 years of production are displayed in **Figures 4e** and **4g**. The low-temperature fluid diffuses outward along the flow paths, while the surrounding formation continuously transfers heat to the fluid through thermal conduction, forming a distinct thermal sweep front between the low-temperature wellbore and the high-temperature reservoir. Correspondingly, the temperature prediction errors shown in **Figures 4f** and **4h**, which display a pronounced annular distribution, indicating that errors are concentrated at the thermal sweep front. The steep temperature gradient in this region reflects the coexistence of strong convection and significant heat conduction, making it more challenging for the physical constraints and equilibrium losses to be simultaneously satisfied.



(a) (b) (c) (d)

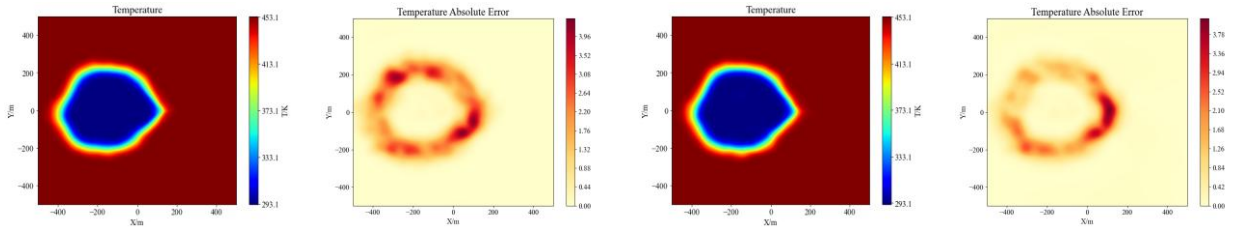


Figure 4. Pressure (a and c) and temperature (e and g) fields, and corresponding pressure (b and d) and temperature (f and h) errors for the doublet-well system, predicted using LHS and LRS.

Figure 5 presents the temperature and pressure fields, as well as their associated prediction errors of the three-well system. The single-well production rate is 0.1 kg/s, and the production-injection balance within the study area is still maintained overall. Compared with the double-well system, the three-well system exhibits a larger overall disturbance range. A comparison between **Figures 5b** and **5d** shows that the application of LRS sampling substantially reduces the error peaks surrounding the injection well. Specifically, the maximum error around the injection well decreases by 20.5% relative to the LHS, demonstrating that local refinement around high-gradient zones can significantly enhance the predictive accuracy of the two-dimensional geothermal reservoir pressure field.

Combined with the analysis of the temperature and temperature error contour maps, it is found that the temperature prediction errors are not only distributed at the temperature front between injection and production wells, but also in regions where the spatial variation of permeability in the heterogeneous reservoir is relatively significant. This phenomenon indicates that abrupt permeability contrasts increase the complexity of streamline structures, making it more difficult for the PDE residual terms in the PINNs framework to simultaneously the constraints of multi-directional strong convection regions. Consequently, the temperature field exhibits local non-smooth behavior, which amplifies the predictive uncertainty of the model. In comparison with LHS, the LRS sampling strategy consistently maintains higher predictive accuracy along the evolving thermal front.

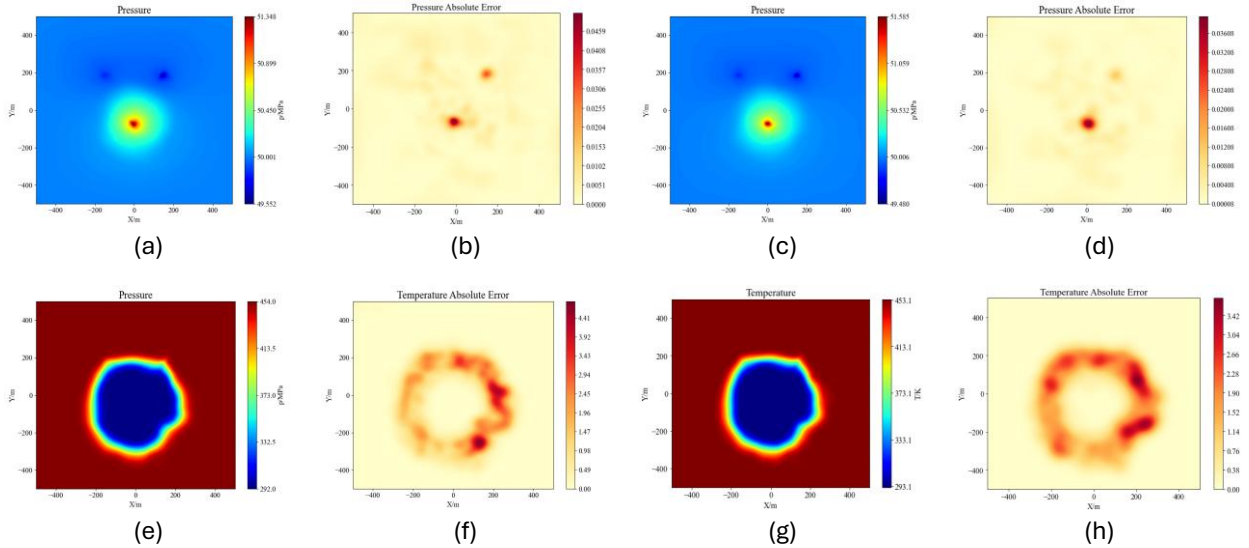


Figure 5. Pressure (a and c) and temperature (e and g) fields, and corresponding pressure (b and d) and temperature (f and h) errors for the three-well system, predicted using LHS and LRS.

The interwell interference within the four-well system further amplifies the spatial complexity of both the pressure and temperature fields, as illustrated in Figure 6. The pressure disturbance and low-temperature swept zones generated by the two injection wells continuously expand and eventually overlap. Although LHS effectively reduces errors in the vicinity of the wellbore, the sampling density remains insufficient in local high-gradient zones, leading to noticeable deviations in the predicted position and morphology of the low-temperature front. Consequently, the improvement in predictive accuracy is limited. In contrast, LRS increases information resolution in these high-gradient regions, substantially suppressing local error peaks near the injection wells and achieving overall lower error magnitudes. These results demonstrate that LRS effectively mitigates the local error accumulation induced by multi-well interference.

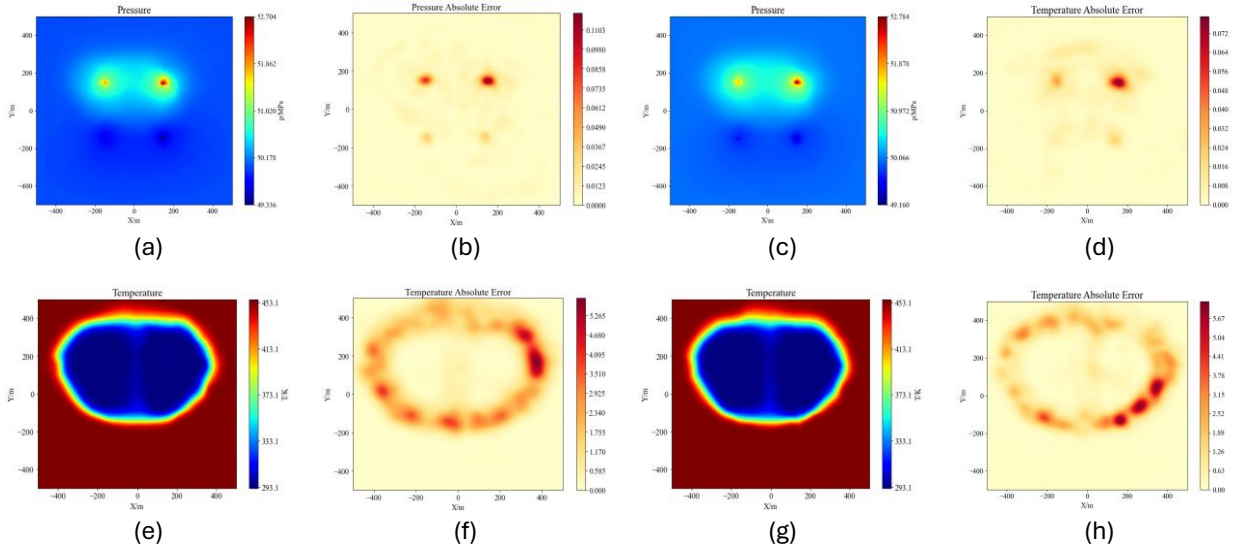


Figure 6. Pressure (a and c) and temperature (e and g) fields, and corresponding pressure (b and d) and temperature (f and h) errors for the four-well system, predicted using using LHS and LRS.

4.3 Model Evaluation Metrics

The performance of the PINNs surrogate model is evaluated by comparing its predicted results with the COMSOL numerical solutions. To quantitatively assess the deviation between the PINNs and the reference solution, the mean absolute error (MAE) and the root mean square error (RMSE) are employed as evaluation metrics to comprehensively characterize the prediction accuracy of the surrogate model. The mathematical definitions are expressed as follows:

$$MAE = \frac{1}{n}\sum_{i=1}^{n}|u_i - \hat{u}_i| \tag{19}$$

$$RMSE = \sqrt{\frac{1}{n}\sum_{i=1}^{n}(u_i - \hat{u}_i)^2} \tag{20}$$

Where u_i denotes the pressure predicted by the PINNs; $\hat{u}_i$ represents the COMSOL numerical solution; n indicates the total number of data samples. Lower MAE and RMSE values indicate higher predictive accuracy.

The pressure evaluation metrics for each case after 20 years of production are listed in **Table 2**. Among the three cases, the MAE of LRS is reduced by 31.2%, 39.7%, and 35.5% compared with LHS, while the RMSE is reduced by 9.8%, 34.8%, and 33.1%, respectively. These results indicate that the locally refined sampling is particularly effective in capturing the sharp pressure gradients throughout the geothermal reservoir production. **Table 3** presents the evaluation metrics for temperature prediction of the two sampling strategies. LRS consistently outperforms LHS, highlighting its robustness in representing complex temperature field geometries. To further assess the surrogate model's capability in resolving localized pressure gradients, **Figure 7** shows the peak injection and production pressures for each case under both sampling methods, compared against the COMSOL numerical solution. The results confirm that LRS captures local high- and low-pressure regions much more accurately than LHS. In Case 3, for example, the maximum injection pressure obtained by COMSOL is 52.84 MPa; LHS predicts 52.70 MPa, whereas LRS further improves the accuracy to 52.78 MPa. In summary, numerous local steep gradients exist in the TH coupled field in geothermal reservoirs. LRS can effectively reduce smoothing errors and consequently enhances the accuracy and reliability of the PINNs surrogate model.

Table 2. Pressure Evaluation metrics after 20 years of production for each case

Case	LHS		LRS	
	MAE/MPa	RMSE/MPa	MAE/MPa	RMSE/MPa
Case 1	0.01911	0.04845	0.01315	0.04371
Case 2	0.02248	0.06348	0.01355	0.04139
Case 3	0.02069	0.07956	0.01334	0.05320

Table 3. Temperature Evaluation metrics after 20 years of production for each case

Case	LHS		LRS	
	MAE/K	RMSE/K	MAE/K	RMSE/K
Case 1	0.823	1.810	0.701	1.500
Case 2	0.678	1.471	0.547	1.429
Case 3	0.815	1.701	0.739	1.642

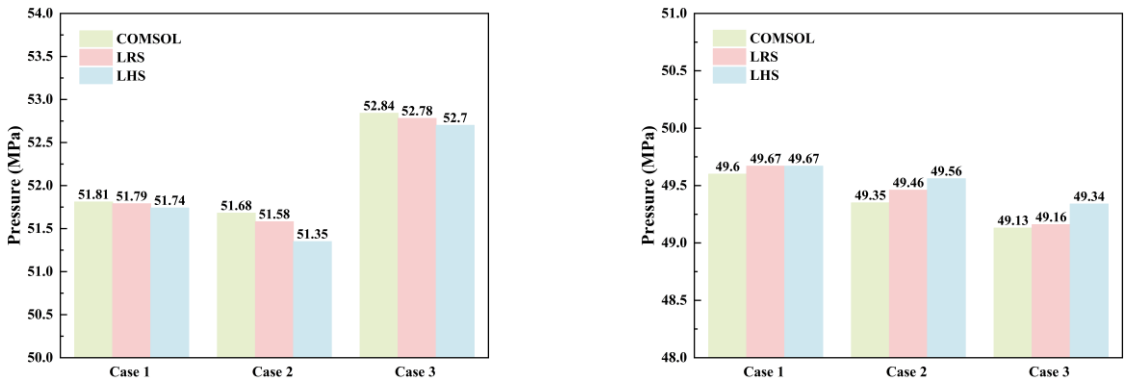


Figure 7. Comparison of PINN predictions using LHS and LRS with numerical simulation results for (a) maximum injection pressure and (b) minimum production pressure.

5 CONCLUSIONS

The study integrates two sampling methods to develop Physics-Informed Neural Networks (PINNs) surrogate model for thermal-hydraulic coupled field, aiming to predict the long-term evolution of temperature and pressure in geothermal reservoirs. The main findings are as follows:

- The model maintains high overall accuracy, with errors mainly occurring in regions featuring strong physical gradients: pressure errors concentrate near the injection and production wells, while temperature errors appear at the low-temperature front. Nonetheless, the surrogate model demonstrates robust predictive reliability across the domain.
- Under the same number of training samples, LRS significantly reduces prediction errors compared to LHS, yielding a minimum pressure prediction error of MAE 0.013 MPa (RMSE 0.04139 MPa) and a temperature MAE of 0.547 K (RMSE 1.429 K). The results demonstrate the advantage of LRS in capturing gradient variations in critical regions.
- The developed surrogate model enables rapid prediction of pressure and temperature in coupled thermal-hydraulic fields without requiring complex mesh generation. Future work will extend the framework to predict reservoir parameters in more heterogeneous and structurally complex geothermal settings.

Acknowledgements

The authors would like to acknowledge the National Natural Science Foundation of China (Grant No. 52304057, No. 52574019, U24B20325, No. 2421002), National Science and Technology Major Project of China (Grant No. 2024ZD1003604), China National Postdoctoral Program for Innovative Talents (Grant No. BX20230428),

National Natural Science Fund for Distinguished Young Scholars of China (Grant No. 52125401), Program of Introducing Talents of Discipline to Chinese Universities (111 Plan) (Grant No. B17045, B25049). Additionally, the Science Foundation of China University of Petroleum, Beijing (Grant No. 2462023XKBH016, 2462024BJRC018) is appreciated.

REFERENCES

Chen, P., Sun, J., Lin, C., and Zhou, W.: Application of the finite volume method for geomechanics calculation and analysis on temperature dependent poromechanical stress and displacement fields in enhanced geothermal system, Geothermics, 95, (2021), 102138.

Ji, J., Zhao, J., Yi, J., Song, X. and Wang, G.: Optimization of hot dry rock heat extraction performance considering the interaction of multi-mineral component water-rock reactions and fracture roughness, Energy, (2025), 135089.

Jagtap, A. D., Kharazmia, E. and Karniadakis G. E.: Conservative physics-informed neural networks on discrete domains for conservation laws: Applications to forward and inverse problems, Computer Methods in Applied Mechanics and Engineering, 365, (2020), 113028.

Li, B., Zhang, J., Yan, H., Zhou, N., Li, M., and Liu, H.: Numerical investigation into the effects of geologic layering on energy performances of thermal energy storage in underground mines, Geothermics, 102, (2022), 102403.

Ma, B., Zhang, C., Zhou, M., Pan, T., Song, X. and Zhu, Z.: Physics-Informed Multitask Learning with Dynamic Weighting for Efficient Prediction of Extended-Reach Wellbore Cleanliness, SPE Journal, SPE-231168-PA, (2025), 1–18.

Mao, Z., Jagtap, A. D. and Karniadakis, G. E.: Physics-informed neural networks for high-speed flows, Computer Methods in Applied Mechanics and Engineering, 360, (2020), 112789.

Raissi, M., Perdikarisb, P. and Karniadakis, G.E.: Physics-informed neural networks: A deep learning framework for solving forward and inverse problems involving nonlinear partial differential equations, Journal of Computational Physics, 378, (2019), 686-707.

Shi, Y., Liu, C., Song X., and Yan, S.: Fourier neural operator-based temperature field prediction model for fractured geothermal reservoirs: addressing diverse fracture morphologies and injection-production parameters, Geothermics,131, (2025), 103404.

Sun, L., Gao, H., Pan, S. and Wang, J.: Surrogate modeling for fluid flows based on physics-constrained deep learning without simulation data, Computer Methods in Applied Mechanics and Engineering, 361, (2020), 112732.

Wang, G., Song, X., Yu, C., Shi, Y., Song, G., Xu, F., Ji, J. and Song, Z.: Heat extraction study of a novel hydrothermal open-loop geothermal system in a multi-lateral horizontal well, Energy, 242, (2022), 122527.

Wei, X., Feng, Z., and Zhao, Y.: Numerical simulation of thermo-hydro-mechanical coupling effect in mining fault-mode hot dry rock geothermal energy, Renewable Energy, 139, (2019), 120-135.

Yang, W., Xiao, C., Zhang, Z. and Liang. X.: Identification of the formation temperature field of the southern Songliao Basin, China based on a deep belief network, Renewable Energy, 182, (2022), 32-42.

Zhang, X., Zhu, Y., Wang, J., Ju, L., Qian, Y., Ye, M., and Yang, J.: GW-PINN: A deep learning algorithm for solving groundwater flow equations, Advances in Water Resources, 165, (2022), 104243.